

RESEARCH ARTICLE

[View Article Online](#)  
[View Journal](#) | [View Issue](#)



Cite this: *Inorg. Chem. Front.*, 2024, **11**, 4770

## Steady Cu<sup>+</sup> species via magnesium and boron co-modification for enhanced CO<sub>2</sub> electroreduction to C<sub>2+</sub> products: an *in situ* Raman spectroscopic study<sup>†</sup>

Hua Yang,<sup>a</sup> Xuefan Mu,<sup>a</sup> Jiexin Guan,<sup>a</sup> Bo Ouyang,<sup>b</sup> Huaming Li<sup>a</sup> and Yilin Deng<sup>a</sup>

The electrochemical carbon dioxide reduction reaction (CO<sub>2</sub>RR) to produce high-value multi-carbon (C<sub>2+</sub>) compounds holds significant practical importance in realizing carbon neutrality. Copper-based electrocatalysts are promising for CO<sub>2</sub>-to-C<sub>2+</sub> conversion. However, the labile Cu valence at high current densities impedes C<sub>2+</sub> product generation. Here, we present an electrocatalyst derived from CuO, featuring a heterostructure of Cu/Cu<sub>2</sub>O/CuO/Mg(OH)<sub>2</sub> via the co-addition of Mg and B during the preparation (referred to as Cu<sub>5</sub>(B<sub>0.02</sub> M)Mg<sub>1</sub>). The Cu<sub>5</sub>(B<sub>0.02</sub> M)Mg<sub>1</sub> shows an impressive C<sub>2+</sub> yield, with a Faraday efficiency (FE<sub>C<sub>2+</sub></sub>) of 79.59% at -1.57 V vs. RHE (reversible hydrogen electrode). Additionally, the partial current density of C<sub>2+</sub> on the Cu<sub>5</sub>(B<sub>0.02</sub> M)Mg<sub>1</sub> catalyst is -317.03 mA cm<sup>-2</sup>, 2.7 and 3.5 times higher than those catalysts lacking B (Cu<sub>5</sub>Mg<sub>1</sub> catalyst) or Mg (Cu(B<sub>0.02</sub> M) catalyst), respectively. Over a wide potential range of 600 mV between -1.17 and -1.77 V vs. RHE, the overall FE<sub>C<sub>2+</sub></sub> surpasses 60% on the Cu<sub>5</sub>(B<sub>0.02</sub> M)Mg<sub>1</sub> catalyst. X-ray diffraction (XRD), X-ray photoelectron spectroscopy (XPS) and high-resolution transmission electron microscopy (HRTEM) characterization studies indicate the NaBH<sub>4</sub> reactant could promote the formation of crystalline Mg(OH)<sub>2</sub> in the catalyst structure, which is found to better stabilize Cu<sup>+</sup> at negative potentials compared to the amorphous phase. Further *in situ* Raman spectroscopy reveals that at increasingly negative potentials, the higher copper species (Cu<sup>2+</sup>) is inevitably reduced to the lower copper species (Cu<sup>0</sup>/Cu<sup>+</sup>). However, the synergy of Mg and B prolongs the presence of Cu<sup>+</sup> on the catalyst surface across a broad potential range, and \*CO and \*CO<sub>2</sub><sup>-</sup> could still be recorded at quite negative reduction potentials. This suggests enhanced binding strength of \*CO intermediates on the catalyst surface, promoting the C-C coupling process.

Received 2nd April 2024,  
Accepted 16th May 2024

DOI: 10.1039/d4qi00842a  
[rsc.li/frontiers-inorganic](http://rsc.li/frontiers-inorganic)

### 1. Introduction

The electrocatalytic carbon dioxide reduction reaction (CO<sub>2</sub>RR) represents a pathway for producing high-value-added chemicals and fuels, offering a means to reduce global carbon dioxide (CO<sub>2</sub>) emissions and alleviate the shortage of non-renewable carbon resources.<sup>1-3</sup> The CO<sub>2</sub>RR yields primarily hydrocarbons and oxygen-containing compounds. Among them, multi-carbon (C<sub>2+</sub>) products such as ethylene (C<sub>2</sub>H<sub>4</sub>) and ethanol (C<sub>2</sub>H<sub>5</sub>OH) have broader industrial applications and higher energy densities compared with C<sub>1</sub> products like

carbon monoxide (CO) and methane (CH<sub>4</sub>), thus commanding a higher economic value per unit mass.<sup>4-6</sup> However, challenges persist due to the requirement of a significant amount of energy to break the C=O bond with the high dissociation energy of CO<sub>2</sub> (about 750 kJ mol<sup>-1</sup>). Furthermore, the multi-step proton-coupling process contributes to the poor selectivity and yield of target products during the CO<sub>2</sub>RR.<sup>7-9</sup> Addressing these issues requires the exploration and design of electrocatalysts with enhanced efficiency to facilitate CO<sub>2</sub> conversion while minimizing product distribution variability during the CO<sub>2</sub>RR process.

To date, copper-based materials, which have been found crucial for C-C coupling, remain the major electrocatalysts for efficiently converting CO<sub>2</sub> to long-chain hydrocarbons and multi-carbon oxygenates.<sup>10-12</sup> Previous studies suggest that Cu<sup>+</sup> species on Cu-based materials could enhance the selectivity of C<sub>2+</sub> products.<sup>13,14</sup> However, under high-current electrolysis, particularly at the negative potentials required for C<sub>2+</sub>

<sup>a</sup>Institute for Energy Research, Jiangsu University, Zhenjiang 212013, China.  
E-mail: [yldeng@ujs.edu.cn](mailto:yldeng@ujs.edu.cn)

<sup>b</sup>Department of Applied Physics and Institution of Energy and Microstructure, Nanjing University of Science and Technology, Nanjing 210094, China

† Electronic supplementary information (ESI) available. See DOI: <https://doi.org/10.1039/d4qi00842a>

product formation, the catalyst structure becomes unstable, and  $\text{Cu}^+$  is readily reduced to  $\text{Cu}^0$  during the  $\text{CO}_2\text{RR}$ . Consequently, prolonging the lifetime of  $\text{Cu}^+$  at reduction potentials is a current research focus. To preserve  $\text{Cu}^+$  during the  $\text{CO}_2\text{RR}$  so as to enhance  $\text{C}_{2+}$  formation, essential steps involve generating  $\text{Cu}^+$  sites and optimizing intermediate adsorption. Researchers have developed several strategies for this purpose, including doping modification,<sup>15,16</sup> addition of different metallic elements,<sup>17,18</sup> heterogeneous interface engineering,<sup>19,20</sup> oxidation state regulation,<sup>21–23</sup> defect control,<sup>21,24–26</sup> etc. Until now, nonmetallic elements such as B, C, F, and S have been reported to effectively regulate the electronic structure and stabilize  $\text{Cu}^+$  in Cu lattices, facilitating the reduction of  $\text{CO}_2$  to  $\text{C}_{2+}$  products at large current densities.<sup>27–29</sup> For example, Yao *et al.* devised a B- $\text{Cu}_2\text{O}$  catalyst which showed high selectivity for ethanol product. Their oxygen programmed desorption and density functional theory (DFT) calculations confirmed that B prevented lattice oxygen from separating out from  $\text{Cu}_2\text{O}$ , thereby stabilizing  $\text{Cu}^+$  species on the B- $\text{Cu}_2\text{O}$  surface. This was believed to strengthen Cu–O bonds, significantly enhancing C–C coupling and facilitating the formation of  $\text{C}_{2+}$  products.<sup>30</sup> Alkaline-earth metals such as Mg, Ba and Ca were found to not only maintain  $\text{Cu}^+$  on catalyst surfaces, but also enhance the adsorption of intermediates at active centers, thereby influencing the reaction kinetics of the  $\text{CO}_2\text{RR}$  process.<sup>31</sup> For instance, Peng *et al.* synthesized a nano- $\text{Cu}_2\text{Mg}$  intermetallic catalyst predominantly oriented along the (111) crystal face on a carbon black substrate (denoted as  $\text{Cu}_2\text{Mg}(111)$ ). *In situ* Raman spectroscopy and DFT calculations confirmed that the  $\text{Cu}_3^{\delta-}\text{Mg}^{\delta+}$  active sites in  $\text{Cu}_2\text{Mg}(111)$  enhanced the coverage of  $^*\text{CO}$  on the catalyst surface, lowered the energy barrier for  $^*\text{CO}$ –CO coupling, and stabilized the  $^*\text{CHCHOH}$  intermediates to promote ethanol production.<sup>32</sup> In addition, Xie *et al.* engineered a Mg-modified  $\text{Cu}_x\text{O}$  nanoparticle catalyst targeting the  $\text{C}_2\text{H}_4$  product. *In situ* XRD, *in situ* Raman spectroscopy and DFT calculations demonstrated that the amorphous  $\text{Mg}(\text{OH})_2$  species stabilized  $\text{Cu}^+$  species, promoting the presence of vital high  $^*\text{CO}$  intermediates for  $\text{C}_{2+}$  products.<sup>33</sup> However, challenges still exist regarding these Cu-based materials specially designed for  $\text{C}_{2+}$  products. Under current modification measures,  $\text{Cu}^+$  has a relatively short lifetime and could only exist within a narrow potential window, significantly limiting its effectiveness during the  $\text{CO}_2\text{RR}$ . Furthermore, there is a lack of literature on the combined effects of alkaline-earth metals and non-metals on copper catalysts. Additionally, the influence of the crystalline or amorphous state of alkaline-earth metal oxides on the stability of  $\text{Cu}^+$  has not been thoroughly studied.

Based on the above considerations, we have designed a B-Cu/ $\text{Cu}_2\text{O}$ / $\text{CuO}$ / $\text{Mg}(\text{OH})_2$  catalyst through a simple two-step protocol involving calcination and wet chemical reduction, aiming to enhance  $\text{C}_{2+}$  products at high current densities across wide potential ranges. The target catalyst is referred to as  $\text{Cu}_5(\text{B}_{0.02} \text{ M})\text{Mg}_1$ , named according to the content of the elements during its preparation. X-ray diffraction (XRD), high-resolution transmission electron microscopy (HRTEM) and *ex*

*situ* X-ray photoelectron spectroscopy (XPS) reveal that the addition of  $\text{NaBH}_4$  during catalyst synthesis could promote the formation of crystalline  $\text{Mg}(\text{OH})_2$  in the catalyst structure, which we suggest would better stabilize  $\text{Cu}^+$  compared to the amorphous  $\text{Mg}(\text{OH})_2$  phase. Further *in situ* Raman investigation confirms that  $\text{Cu}^+$  on the  $\text{Cu}_5(\text{B}_{0.02} \text{ M})\text{Mg}_1$  catalyst could persist across a much broader potential window compared to those catalysts lacking crystalline  $\text{Mg}(\text{OH})_2$  or B. Additionally, the  $^*\text{CO}$  intermediate, a significant precursor of  $\text{C}_{2+}$  products, is recorded on the  $\text{Cu}_5(\text{B}_{0.02} \text{ M})\text{Mg}_1$  surface even at rather negative potentials during the  $\text{CO}_2\text{RR}$ . Benefiting from the stabilized  $\text{Cu}^+$ ,  $\text{Cu}_5(\text{B}_{0.02} \text{ M})\text{Mg}_1$  shows high selectivity towards  $\text{C}_{2+}$  within  $-1.17$  to  $-1.77$  V *vs.* RHE (unless specified, all potentials in this work are referenced against RHE). Overall, our work reveals the significance of morphologies of  $\text{Mg}(\text{OH})_2$  in  $\text{Cu}^+$  stabilization and provides a comprehensive understanding of the role of  $\text{Cu}^+$  in the efficient  $\text{CO}_2\text{RR}$  towards  $\text{C}_{2+}$  products.

## 2. Results and discussion

### 2.1 Morphological and structural characterization of the catalysts

The typical fabrication process of  $\text{Cu}_5(\text{B}_{0.02} \text{ M})\text{Mg}_1$  is depicted in Fig. 1, with detailed synthesis described in the ESI.† The XRD pattern indicates diffraction peaks of Cu,  $\text{Cu}_2\text{O}$ ,  $\text{CuO}$  and  $\text{Mg}(\text{OH})_2$  in the  $\text{Cu}_5(\text{B}_{0.02} \text{ M})\text{Mg}_1$  catalyst (Fig. 2a). The characteristic peaks at  $42.3^\circ$ ,  $50.4^\circ$ , and  $74.1^\circ$  correspond to the (111), (200) and (220) planes of Cu (PDF#04-0836), respectively. Additionally, four peaks at  $29.5^\circ$ ,  $36.4^\circ$ ,  $42.3^\circ$  and  $61.3^\circ$  correspond to the (110), (111), (200) and (220) planes of  $\text{Cu}_2\text{O}$  (PDF#05-0667), respectively. Peaks at  $35.4^\circ$ ,  $39.7^\circ$ ,  $48.7^\circ$ ,  $53.5^\circ$  and  $66.4^\circ$  are attributed to the (002), (111), (202), (020) and (310) planes of  $\text{CuO}$  (PDF#48-1548), respectively. Furthermore, peaks at  $18.5^\circ$ ,  $32.9^\circ$ ,  $58.6^\circ$  and  $68.2^\circ$  align well with the (001), (100), (110) and (103) planes of  $\text{Mg}(\text{OH})_2$  (PDF#44-1482), respectively. The XRD pattern demonstrates that the  $\text{Cu}_5(\text{B}_{0.02} \text{ M})\text{Mg}_1$  catalyst mainly comprises Cu,  $\text{Cu}_2\text{O}$ ,  $\text{CuO}$  and  $\text{Mg}(\text{OH})_2$  crystal phases. On the other hand, XRD patterns of the corresponding reference  $\text{Cu}_5\text{Mg}_1$ ,  $\text{Cu}_5(\text{B}_{0.1} \text{ M})\text{Mg}_1$ ,  $\text{Cu}(\text{B}_{0.02} \text{ M})$ ,  $\text{Cu}_{10}(\text{B}_{0.02} \text{ M})\text{Mg}_1$  and  $\text{Cu}_1(\text{B}_{0.02} \text{ M})\text{Mg}_1$  catalysts are provided in Fig. S1.† The  $\text{Cu}_5(\text{B}_{0.1} \text{ M})\text{Mg}_1$ ,  $\text{Cu}_{10}(\text{B}_{0.02} \text{ M})\text{Mg}_1$  and  $\text{Cu}_1(\text{B}_{0.02} \text{ M})\text{Mg}_1$  catalysts also consist of Cu,  $\text{Cu}_2\text{O}$ ,  $\text{CuO}$  and  $\text{Mg}(\text{OH})_2$ . The  $\text{Cu}(\text{B}_{0.02} \text{ M})$  catalyst comprises three phases: Cu,  $\text{Cu}_2\text{O}$  and  $\text{CuO}$ . Notably, for the  $\text{Cu}_5\text{Mg}_1$  catalyst (lacking the  $\text{NaBH}_4$  reactant during its preparation), XRD only reveals the existence of  $\text{CuO}$  (PDF#48-1548), while the  $\text{Mg}(\text{OH})_2$  (PDF#44-1482) crystalline phases are absent. We propose that this results from the generation of amorphous  $\text{Mg}(\text{OH})_2$  rather than crystalline  $\text{Mg}(\text{OH})_2$  when the reducing agent  $\text{NaBH}_4$  is absent (Fig. S1a†).<sup>34</sup>

Scanning electron microscopy (SEM) and TEM reveal that the as-prepared  $\text{Cu}_5(\text{B}_{0.02} \text{ M})\text{Mg}_1$  catalyst is constructed of nanoclusters (Fig. S2† and Fig. 2b). Energy-dispersive X-ray spectroscopy (EDS) elemental mappings demonstrate a uniform distribution of Cu, Mg, B and O elements on the cata-

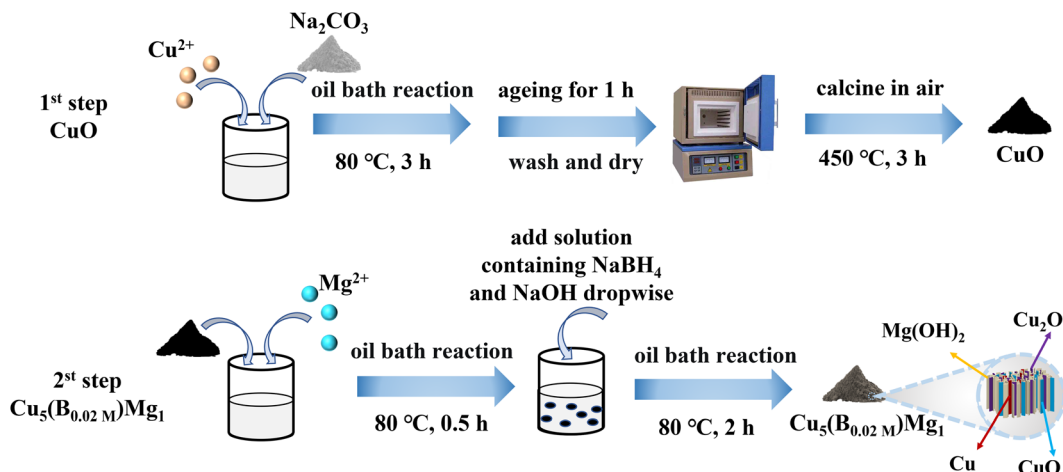


Fig. 1 Graphical scheme for the synthesis of the  $\text{Cu}_5(\text{B}_{0.02\text{ M}})\text{Mg}_1$  catalyst.

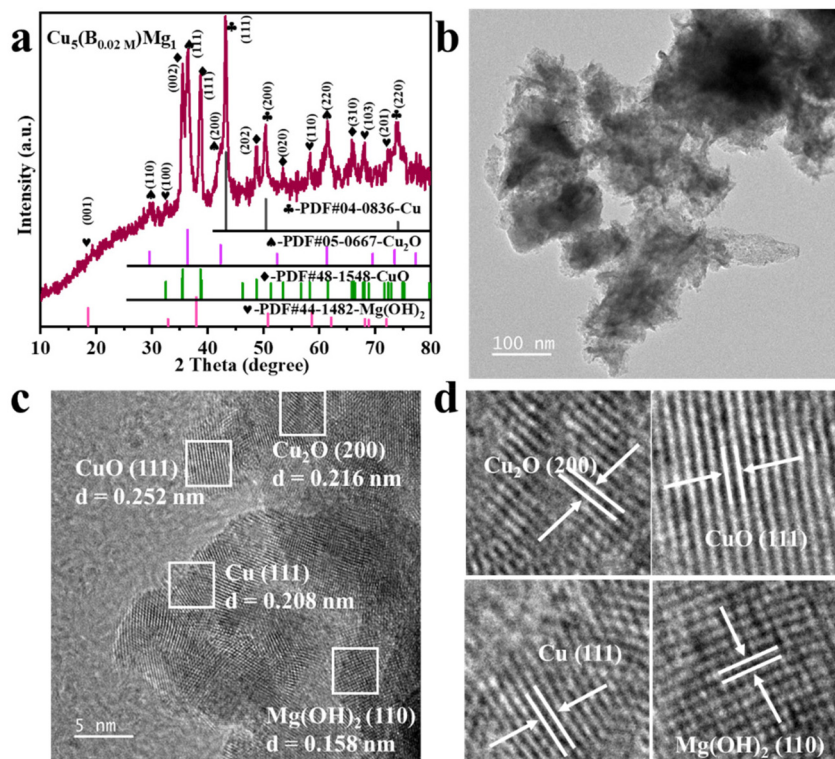


Fig. 2 (a) XRD, (b) TEM and (c) HRTEM characterization of the  $\text{Cu}_5(\text{B}_{0.02\text{ M}})\text{Mg}_1$  catalyst. (d) is the enlarged view of (c).

lyst surface (Fig. S2c and d†). SEM and EDS characterization studies were performed on the  $\text{Cu}_5\text{Mg}_1$ ,  $\text{Cu}_5(\text{B}_{0.1\text{ M}})\text{Mg}_1$ ,  $\text{Cu}(\text{B}_{0.02\text{ M}})$ ,  $\text{Cu}_{10}(\text{B}_{0.02\text{ M}})\text{Mg}_1$  and  $\text{Cu}_1(\text{B}_{0.02\text{ M}})\text{Mg}_1$  catalysts as well, with the corresponding results shown in Fig. S3–S7.† Further HRTEM analysis reveals interplanar spacings of 0.208 (Cu (111)), 0.216 ( $\text{Cu}_2\text{O}$  (200)), 0.252 (CuO (111)) and 0.158 nm ( $\text{Mg}(\text{OH})_2$  (110)) in the  $\text{Cu}_5(\text{B}_{0.02\text{ M}})\text{Mg}_1$  catalyst, consistent with its XRD result (Fig. 2c and d). TEM and HRTEM were also conducted on  $\text{Cu}(\text{B}_{0.02\text{ M}})$  and  $\text{Cu}_5\text{Mg}_1$  to explore the effect of

Mg and B on the structure of the catalyst (Fig. S8 and S9†). For the  $\text{Cu}(\text{B}_{0.02\text{ M}})$  catalyst, the HRTEM image reveals crystal lattices with interfacial spacings of 0.209, 0.247, and 0.253 nm, coinciding with the Cu (111),  $\text{Cu}_2\text{O}$  (111), and CuO (111) lattices (Fig. S8†). Conversely, the  $\text{Cu}_5\text{Mg}_1$  catalyst primarily exhibits the CuO (111) crystalline phase, along with some amorphous species (Fig. S9†). Considering TEM and XRD results collectively, we may speculate that the observed amorphous substance in  $\text{Cu}_5\text{Mg}_1$  arises from some Mg-based amorphous

species formed due to the absence of the  $\text{NaBH}_4$  reagent (Fig. S9b†).

The electronic structures of the catalysts with different ratios of Cu, Mg and B additions were characterized by XPS (Fig. 3). The Cu 2p XPS spectra demonstrate two peaks corresponding to Cu 2p<sub>3/2</sub> and Cu 2p<sub>1/2</sub> (Fig. 3a and b).<sup>35,36</sup> The peaks at 933.98 and 953.78 eV are attributed to the Cu<sup>2+</sup> of CuO in  $\text{Cu}_5\text{Mg}_1$  (Fig. 3a and Table S1†),<sup>37-39</sup> indicating that in the absence of  $\text{NaBH}_4$  reducing agent, the Cu species in the catalyst mainly exists in the form of Cu<sup>2+</sup>. Notably, upon  $\text{NaBH}_4$  addition, the Cu<sup>2+</sup> bands of  $\text{Cu}_5(\text{B}_{0.02} \text{ M})\text{Mg}_1$  and  $\text{Cu}_5(\text{B}_{0.1} \text{ M})\text{Mg}_1$  catalysts shift to higher electron binding energies by 0.55 and 0.64 eV, respectively, and at the same time Cu<sup>0</sup>/Cu<sup>+</sup> is produced. Additionally, with increasing  $\text{NaBH}_4$  content, the Cu<sup>0</sup>/Cu<sup>+</sup> electron binding energies decrease from 932.43/952.23 eV ( $\text{Cu}_5(\text{B}_{0.02} \text{ M})\text{Mg}_1$ ) to 932.17/951.97 eV ( $\text{Cu}_5(\text{B}_{0.1} \text{ M})\text{Mg}_1$ ) (Fig. 3a and Table S1†).<sup>40-42</sup> These results demonstrate that the  $\text{NaBH}_4$  content is a key factor affecting the electronic structure of Cu centers. To further differentiate between Cu<sup>0</sup> and Cu<sup>+</sup>, Cu LMM Auger electron spectroscopy analysis was performed on  $\text{Cu}_5(\text{B}_{0.02} \text{ M})\text{Mg}_1$  and  $\text{Cu}_5(\text{B}_{0.1} \text{ M})\text{Mg}_1$  catalysts (Fig. S10†). The two peaks at around 568.00 and 569.75 eV correspond to Cu<sup>0</sup> and Cu<sup>+</sup>,<sup>43,44</sup> respectively, confirming the co-existence of Cu<sup>0</sup> and Cu<sup>+</sup> species on these two catalysts. According to previous studies, Cu<sup>0</sup> and Cu<sup>+</sup> played different roles during the CO<sub>2</sub>RR. Cu<sup>0</sup> contributed to activating

CO<sub>2</sub> molecules.<sup>45</sup> At the initial stage of the reaction, CO<sub>2</sub> tended to be above the Cu<sup>0</sup> zone. After CO<sub>2</sub> activation, Cu<sup>δ+</sup> (0 < δ ≤ 1) was proposed to stabilize CO<sub>2</sub> molecules, which can promote the dimerization process between \*CO intermediates and enhance the subsequent C–C coupling.<sup>46,47</sup> In addition, we have investigated the effects of Mg on the valence state of Cu compounds, as provided in Fig. 3b and Table S2.† It can be seen that Mg plays a similar role to B, since with the increasing Mg content, the characteristic XPS band of Cu<sup>2+</sup> shifts to a higher electron binding energy, while the Cu<sup>0</sup>/Cu<sup>+</sup> peak shifts in the opposite direction. These results suggest that the introduced B and Mg elements interact with the surrounding atoms, altering the electron density at the Cu sites. Fig. 3c shows that regardless of the presence of NaBH<sub>4</sub>, the Mg(OH)<sub>2</sub> species persists on the catalysts, as indicated by its characteristic peak at ~1303.60 eV.<sup>48</sup> Taking the XPS and the above XRD/TEM results into comprehensive consideration, it is suggested that the NaBH<sub>4</sub> reactant plays a significant role in tuning the crystalline state of the Mg(OH)<sub>2</sub> species. In the absence of NaBH<sub>4</sub>, Mg(OH)<sub>2</sub> exists in an amorphous phase, while with NaBH<sub>4</sub> addition, Mg(OH)<sub>2</sub> exists as crystals. We propose that the existing form of Mg(OH)<sub>2</sub> could be a critical influencing factor on the CO<sub>2</sub>RR performance of the catalyst. Nonetheless, the high-resolution B 1s spectra of  $\text{Cu}_5(\text{B}_{0.02} \text{ M})\text{Mg}_1$  and  $\text{Cu}_5(\text{B}_{0.1} \text{ M})\text{Mg}_1$  show two peaks at 191.92 and 191.81 eV, belonging to B–O (Fig. 3d).<sup>49,50</sup> Additionally, the contents

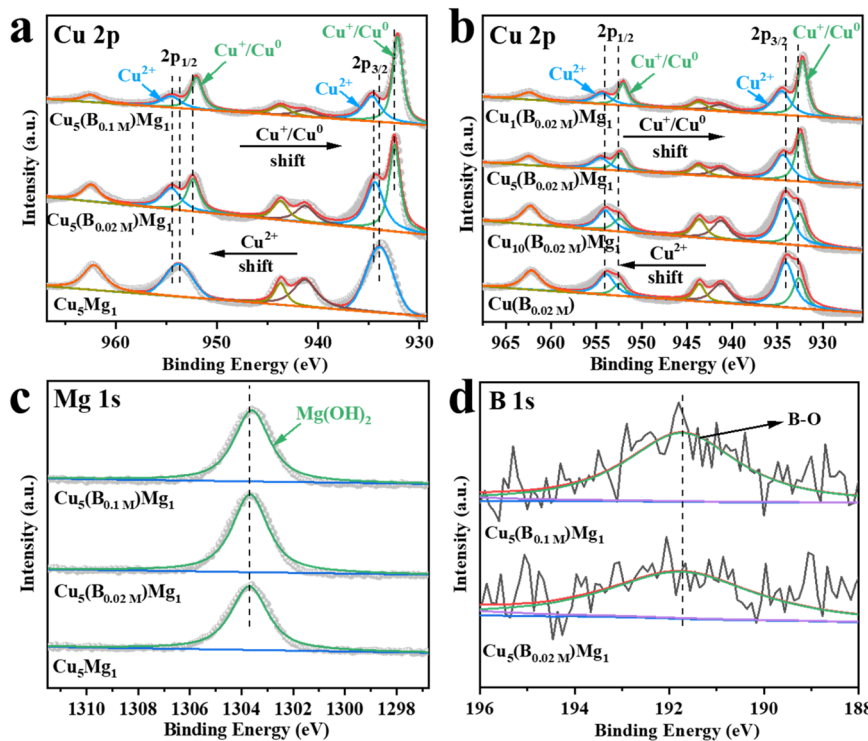


**Fig. 3** XPS spectra of Cu 2p in (a)  $\text{Cu}_5\text{Mg}_1$ ,  $\text{Cu}_5(\text{B}_{0.02} \text{ M})\text{Mg}_1$ ,  $\text{Cu}_5(\text{B}_{0.1} \text{ M})\text{Mg}_1$  (varying the  $\text{NaBH}_4$  feeding amount while keeping the Cu/Mg ratio at 5 : 1) and (b)  $\text{Cu}(\text{B}_{0.02} \text{ M})$ ,  $\text{Cu}_{10}(\text{B}_{0.02} \text{ M})\text{Mg}_1$ ,  $\text{Cu}_5(\text{B}_{0.02} \text{ M})\text{Mg}_1$  and  $\text{Cu}_1(\text{B}_{0.02} \text{ M})\text{Mg}_1$  (varying the ratio of Cu/Mg while keeping the NaBH<sub>4</sub> feeding amount the same at 0.02 M). (c) XPS spectra of Mg 1s in  $\text{Cu}_5\text{Mg}_1$ ,  $\text{Cu}_5(\text{B}_{0.02} \text{ M})\text{Mg}_1$ , and  $\text{Cu}_5(\text{B}_{0.1} \text{ M})\text{Mg}_1$ . (d) The corresponding B 1s XPS spectra of  $\text{Cu}_5(\text{B}_{0.02} \text{ M})\text{Mg}_1$  and  $\text{Cu}_5(\text{B}_{0.1} \text{ M})\text{Mg}_1$  catalysts.

of Cu, Mg and B elements on the  $\text{Cu}_5(\text{B}_{0.02} \text{ M})\text{Mg}_1$  catalyst surface were determined *via* XPS analysis, as provided in Table S3.<sup>†</sup>

## 2.2 Electrochemical $\text{CO}_2$ RR performance in a flow cell

The  $\text{CO}_2$ RR performances of  $\text{Cu}_5(\text{B}_{0.02} \text{ M})\text{Mg}_1$ ,  $\text{Cu}_5(\text{B}_{0.1} \text{ M})\text{Mg}_1$ ,  $\text{Cu}_5\text{Mg}_1$ ,  $\text{Cu}_{10}(\text{B}_{0.02} \text{ M})\text{Mg}_1$ ,  $\text{Cu}_4(\text{B}_{0.02} \text{ M})\text{Mg}_1$  and  $\text{Cu}(\text{B}_{0.02} \text{ M})$  catalysts were evaluated in 1.0 M KOH electrolyte saturated with  $\text{CO}_2$  at potentials ranging from  $-0.77$  to  $-1.97$  V. Typical gaseous products ( $\text{C}_2\text{H}_4$ ,  $\text{CH}_4$ , CO, and  $\text{H}_2$ ) and liquid products ( $\text{CH}_3\text{CH}_2\text{OH}$ ,  $\text{CH}_3\text{COOH}$ ,  $\text{CH}_3\text{OH}$ , and  $\text{HCOOH}$ ) were analyzed (Fig. S11 and S12<sup>†</sup>). Among these different materials,  $\text{Cu}_5(\text{B}_{0.02} \text{ M})\text{Mg}_1$  ( $\text{Cu} : \text{Mg} = 5 : 1$ ,  $\text{NaBH}_4 = 0.02$  M) shows excellent selectivity towards  $\text{C}_{2+}$  products (Fig. 4 and S13<sup>†</sup>).

Linear sweep voltammetry (LSV) was first employed to determine the current densities of these Cu catalysts modified by Mg and/or B under  $\text{CO}_2$ RR conditions (Fig. 4a). It is found that the  $\text{Cu}_5(\text{B}_{0.02} \text{ M})\text{Mg}_1$  catalyst exhibits a significantly higher current density as compared to the  $\text{Cu}_5\text{Mg}_1$  and  $\text{Cu}(\text{B}_{0.02} \text{ M})$  catalysts, suggesting a potentially better  $\text{CO}_2$ RR activity. The electrocatalytic products of the three catalysts were then collected during chronoamperometry measurements, and their Faraday efficiencies (FEs) are presented in Fig. 4b-d. Among all the catalysts,  $\text{Cu}_5(\text{B}_{0.02} \text{ M})\text{Mg}_1$  shows the highest  $\text{C}_{2+}$

product selectivity (Fig. 4b). Notably, the  $\text{FE}_{\text{C}_{2+}}$  for the  $\text{Cu}_5(\text{B}_{0.02} \text{ M})\text{Mg}_1$  catalyst remains  $>60\%$  across a wide potential range of 600 mV (from  $-1.17$  to  $-1.77$  V), significantly outperforming  $\text{Cu}_5\text{Mg}_1$  and  $\text{Cu}(\text{B}_{0.02} \text{ M})$  (Fig. 4b-d). It should be noted that the  $\text{Cu}_5(\text{B}_{0.02} \text{ M})\text{Mg}_1$  catalyst also shows a low FE for  $\text{H}_2$  ( $\text{FE}_{\text{H}_2}$ ) of  $<15\%$  within the potential range of  $-0.77$  to  $-1.57$  V, indicating that the hydrogen evolution reaction is effectively inhibited on the catalyst. In particular, a maximal  $\text{FE}_{\text{C}_{2+}}$  of 79.59% at  $-1.57$  V is recorded for  $\text{Cu}_5(\text{B}_{0.02} \text{ M})\text{Mg}_1$  ( $\text{FE}_{\text{C}_2\text{H}_4} = 50.31\%$ ,  $\text{FE}_{\text{C}_2\text{H}_5\text{OH}} = 28.58\%$ , with a small amount of  $\text{CH}_3\text{COOH}$ ), significantly higher than those of  $\text{Cu}_5\text{Mg}_1$  ( $\text{FE}_{\text{C}_{2+}} = 49.53\%$ ) and  $\text{Cu}(\text{B}_{0.02} \text{ M})$  catalysts ( $\text{FE}_{\text{C}_{2+}} = 31.21\%$ ) (Fig. 5a and Table S4<sup>†</sup>). Furthermore,  $\text{Cu}_5(\text{B}_{0.02} \text{ M})\text{Mg}_1$  shows prominently enhanced partial current densities for  $\text{C}_{2+}$  products ( $j_{\text{C}_{2+}}$ ). As depicted in Fig. 5b,  $j_{\text{C}_{2+}}$  of  $\text{Cu}_5(\text{B}_{0.02} \text{ M})\text{Mg}_1$  ( $-317.03 \text{ mA cm}^{-2}$ ) is 2.7 and 3.5 times higher than those of  $\text{Cu}_5\text{Mg}_1$  ( $-116.74 \text{ mA cm}^{-2}$ ) and  $\text{Cu}(\text{B}_{0.02} \text{ M})$  ( $-91.09 \text{ mA cm}^{-2}$ ) at the same working potential of  $-1.57$  V, suggesting the synergistic promotion of  $\text{C}_{2+}$  formation on Cu surfaces by Mg and B. In addition,  $j_{\text{C}_{2+}}$  of  $\text{Cu}_5(\text{B}_{0.02} \text{ M})\text{Mg}_1$ ,  $\text{Cu}_5\text{Mg}_1$  and  $\text{Cu}(\text{B}_{0.02} \text{ M})$  at more different voltages are shown in Table S5.<sup>†</sup> Additionally, we have investigated the influence of different ratios of B and Mg during preparation on the electrocatalytic  $\text{CO}_2$ RR activities of the catalysts (Fig. S13<sup>†</sup>). The results reveal that appropriate amounts of

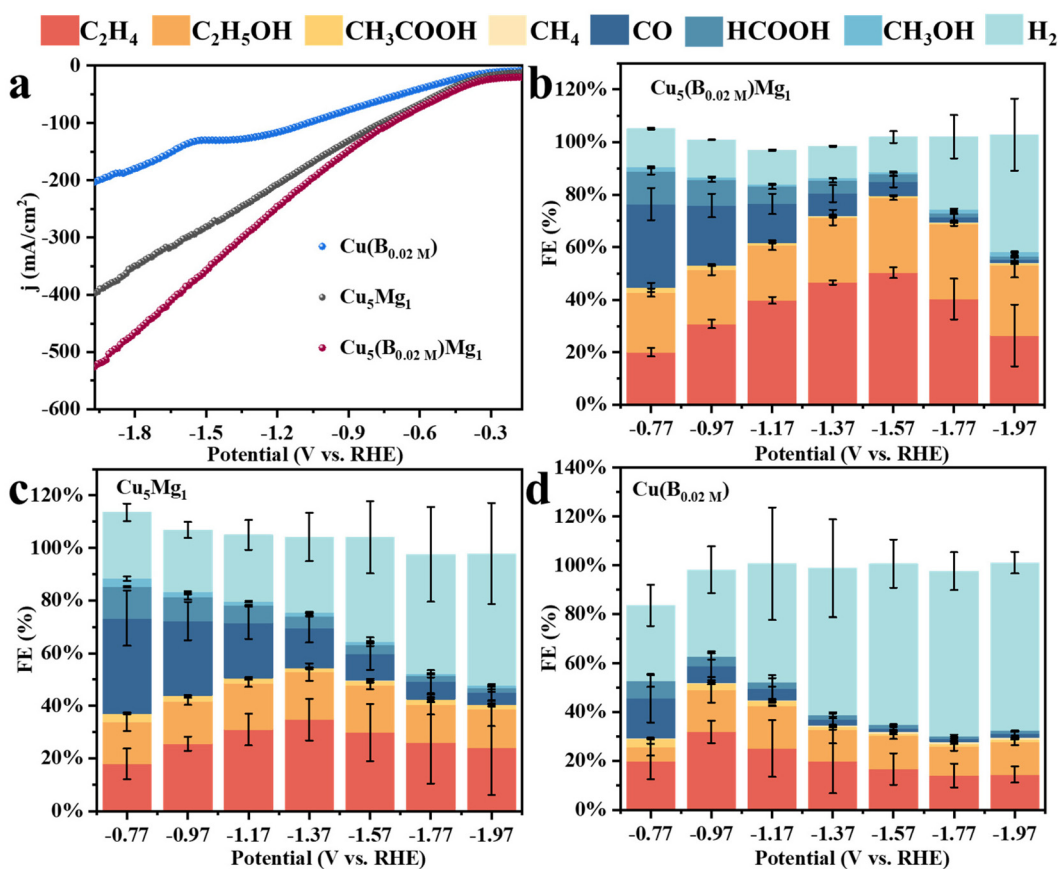


**Fig. 4** (a) LSVs of  $\text{Cu}(\text{B}_{0.02} \text{ M})$ ,  $\text{Cu}_5\text{Mg}_1$  and  $\text{Cu}_5(\text{B}_{0.02} \text{ M})\text{Mg}_1$ . The Faraday efficiencies (FEs) of all products for different catalysts: (b)  $\text{Cu}_5(\text{B}_{0.02} \text{ M})\text{Mg}_1$ , (c)  $\text{Cu}_5\text{Mg}_1$ , and (d)  $\text{Cu}(\text{B}_{0.02} \text{ M})$ .

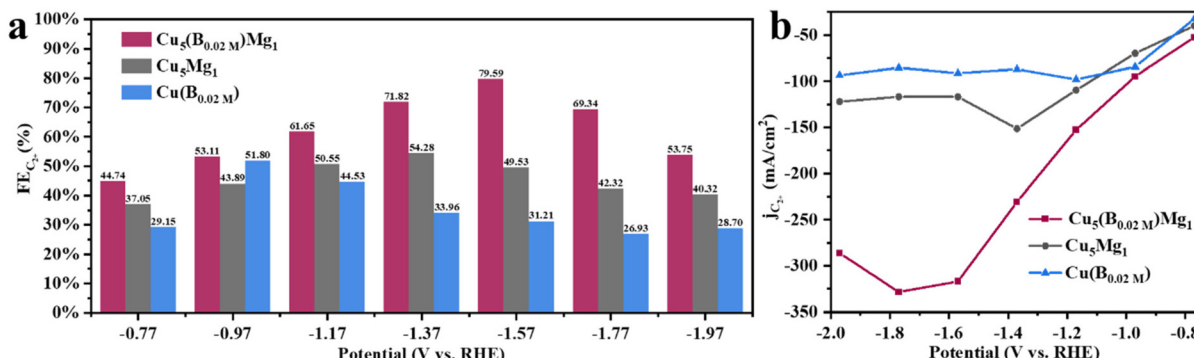


**Fig. 5** Electrochemical CO<sub>2</sub>RR performance of the Cu<sub>5</sub>(B<sub>0.02</sub> M)Mg<sub>1</sub> catalyst: (a) FE<sub>s</sub> of C<sub>2+</sub> (C<sub>2</sub>H<sub>4</sub>, C<sub>2</sub>H<sub>5</sub>OH and CH<sub>3</sub>COOH) at different potentials and (b) partial current densities of C<sub>2+</sub>.

NaBH<sub>4</sub> and Mg reactants during synthesis are conducive to enhanced C<sub>2+</sub> selectivity, while excessive usage will reduce C<sub>2+</sub> products. This could be because the selective promoting and blocking effects of these elements in Cu<sub>5</sub>(B<sub>0.02</sub> M)Mg<sub>1</sub> reach a relatively balanced state for efficient CO<sub>2</sub>RR catalysis (Table S4†).<sup>33</sup> Furthermore, we have compared the CO<sub>2</sub>RR activities of Cu<sub>5</sub>(B<sub>0.02</sub> M)Mg<sub>1</sub> with other different catalysts in previous literature, which shows that the synergy of Mg and B contributes to a competitive selectivity towards C<sub>2+</sub> products (Table S6†).

The long-term catalytic performance of Cu<sub>5</sub>(B<sub>0.02</sub> M)Mg<sub>1</sub> for the CO<sub>2</sub>RR was measured through chronoamperometry at -1.57 V (Fig. S14†). Within a 10 h period, the current density shows negligible attenuation, but the yield of C<sub>2</sub>H<sub>4</sub> gradually decreases over time. After the long-term CO<sub>2</sub>RR measurement, Cu<sub>5</sub>(B<sub>0.02</sub> M)Mg<sub>1</sub> was subjected to XRD characterization. The results indicate that the bulk of the catalyst post CO<sub>2</sub>RR is primarily composed of Cu (PDF#04-0836), Cu<sub>2</sub>O (PDF#05-0667) and Mg(OH)<sub>2</sub> (PDF#44-1482), with CuO completely reduced. Notably, the XRD peaks of Mg(OH)<sub>2</sub> diminish post CO<sub>2</sub>RR, which we believe leads to the decline in the stability of Cu<sub>5</sub>(B<sub>0.02</sub> M)Mg<sub>1</sub> (Fig. S15†). Besides, previous literature studies have suggested that the accumulation of impurities like NO<sub>x</sub>, SO<sub>x</sub>, and carbon on the catalyst surface can also affect the active sites for the CO<sub>2</sub>RR, thereby resulting in a gradual decrease in performance.<sup>51–53</sup> In addition to XRD, XPS characterization was employed to analyze the elemental distribution on the Cu<sub>5</sub>(B<sub>0.02</sub> M)Mg<sub>1</sub> catalyst surface (Fig. S16†). As depicted in Fig. S16a,† copper species, in the form of Cu<sup>0</sup> and Cu<sup>+</sup>, predominantly exist on the catalyst surface. The crystalline Mg(OH)<sub>2</sub> species nearly vanishes after the long-term CO<sub>2</sub>RR, therefore contributing to the decline in the performance of the Cu<sub>5</sub>(B<sub>0.02</sub> M)Mg<sub>1</sub> catalyst (Fig. S16b†). Additionally, XPS results show that the B element still exists on the catalyst (Fig. S16c†).

To study the enhanced CO<sub>2</sub>RR performance of the Cu<sub>5</sub>(B<sub>0.02</sub> M)Mg<sub>1</sub> catalyst, the electrochemically active surface areas of all the electrocatalysts were estimated by calculating their double layer capacitances (C<sub>dl</sub>) (Fig. S17 and S18†). Obviously, compared with Cu<sub>5</sub>Mg<sub>1</sub> (2.83 mF cm<sup>-2</sup>), Cu<sub>5</sub>(B<sub>0.1</sub> M)

Mg<sub>1</sub> (1.61 mF cm<sup>-2</sup>), Cu(B<sub>0.02</sub> M) (0.99 mF cm<sup>-2</sup>), Cu<sub>10</sub>(B<sub>0.02</sub> M)Mg<sub>1</sub> (2.20 mF cm<sup>-2</sup>) and Cu<sub>1</sub>(B<sub>0.02</sub> M)Mg<sub>1</sub> (1.19 mF cm<sup>-2</sup>), Cu<sub>5</sub>(B<sub>0.02</sub> M)Mg<sub>1</sub> (3.28 mF cm<sup>-2</sup>) has the largest C<sub>dl</sub> value, revealing that the Cu<sub>5</sub>(B<sub>0.02</sub> M)Mg<sub>1</sub> catalyst can provide more active sites for the CO<sub>2</sub>RR. Meanwhile, it is worth noting that the active surface area of Cu<sub>5</sub>Mg<sub>1</sub> is lower than that of Cu<sub>5</sub>(B<sub>0.02</sub> M)Mg<sub>1</sub>, which may be due to the formation of amorphous Mg(OH)<sub>2</sub> on the catalyst surface, causing part of the active sites to be covered due to the “stacking” effect, thus reducing the overall catalytic activity of Cu<sub>5</sub>Mg<sub>1</sub>.<sup>54</sup> Electrochemical impedance spectroscopy measurements have also been performed to investigate the charge transfer properties of the catalysts (Fig. S19†). It is obvious that an appropriate co-modification of Mg and B could accelerate the charge transfer process during the CO<sub>2</sub>RR.

*In situ* Raman spectroscopy was further conducted to examine the effects of B and/or Mg on the valence of Cu (Cu<sup>0</sup>, Cu<sup>+</sup> or Cu<sup>2+</sup>) as well as to probe probable intermediates during the CO<sub>2</sub>RR (Fig. 6). Fig. 6a presents the *in situ* Raman spectra of the Cu<sub>5</sub>(B<sub>0.02</sub> M)Mg<sub>1</sub> catalyst in 1.0 M KOH electrolyte (saturated with CO<sub>2</sub>) during the CO<sub>2</sub>RR. At the open circuit voltage, three characteristic peaks are observed at around 147, 522 and 626 cm<sup>-1</sup>, attributed to Cu<sub>2</sub>O.<sup>55–57</sup> After applying a cathodic potential of -0.37 V, a new Raman band appears at 703 cm<sup>-1</sup> on the Cu<sub>5</sub>(B<sub>0.02</sub> M)Mg<sub>1</sub> catalyst, corresponding to surface δCO<sub>2</sub><sup>-</sup>, which represents the umbrella motion of oxygen atoms of the \*CO<sub>2</sub><sup>-</sup> intermediate. Previous studies recognized \*CO<sub>2</sub><sup>-</sup> as the initial intermediate just after CO<sub>2</sub> activation.<sup>58</sup> At the same time, Raman peaks at 290 and 374 cm<sup>-1</sup> are recorded, assigned to the frustrated rotation and tensile vibrations of Cu-CO, respectively.<sup>59–61</sup> Besides, the band at 1071 cm<sup>-1</sup> corresponds to the symmetric C-O stretching band of CO<sub>3</sub><sup>2-</sup> from the electrolyte.<sup>62,63</sup> It is worth noting that over the wide potential range of -0.37 to -1.37 V, Cu<sub>2</sub>O peaks at 147, 522 and 626 cm<sup>-1</sup> consistently appear on the Cu<sub>5</sub>(B<sub>0.02</sub> M)Mg<sub>1</sub> catalyst, indicating that the CuO species on the catalyst surface has been completely reduced, while Cu<sup>+</sup> persists, probably being the reactive sites during the electrochemical CO<sub>2</sub>RR. We propose that the robust stability of Cu<sub>2</sub>O species over a wide potential window is attributed to the synergy of B and crystal-

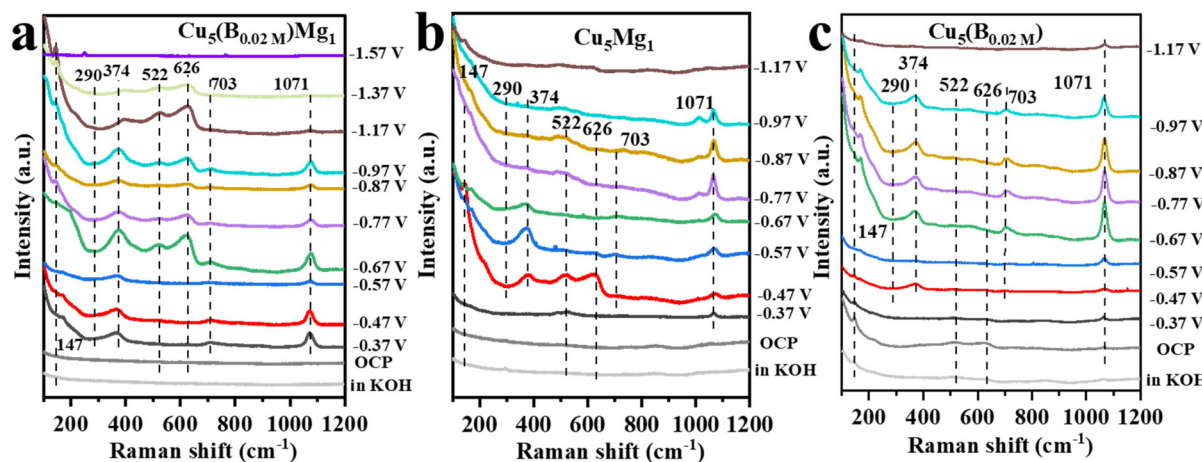


**Fig. 6** The *in situ* Raman spectra of (a)  $\text{Cu}_5(\text{B}_{0.02\text{ M}})\text{Mg}_1$ , (b)  $\text{Cu}_5\text{Mg}_1$  and (c)  $\text{Cu}(\text{B}_{0.02\text{ M}})$  catalysts at various potentials in 1.0 M KOH electrolyte during  $\text{CO}_2\text{RR}$  catalysis.

line  $\text{Mg}(\text{OH})_2$ . According to previous literature, the  $\text{Cu}^+$  on the catalyst surface is crucial for the formation of multi-carbon products.<sup>64–67</sup> The Raman spectra over  $-1.37\text{ V}$  cannot be collected because of the accumulation of gaseous products on the catalyst surface that block signals. Nevertheless, Raman signals for  $\text{Cu}_5\text{Mg}_1$  and  $\text{Cu}(\text{B}_{0.02\text{ M}})$  are also recorded under the same conditions as  $\text{Cu}_5(\text{B}_{0.02\text{ M}})\text{Mg}_1$  to explore the influences of Mg and B on the Cu catalysts, as shown in Fig. 6b and c. In contrast to the  $\text{Cu}_5(\text{B}_{0.02\text{ M}})\text{Mg}_1$  catalyst,  $\text{Cu}_2\text{O}$  peaks vanish at only  $-0.87\text{ V}$  and  $-0.97\text{ V}$  for  $\text{Cu}_5\text{Mg}_1$  and  $\text{Cu}(\text{B}_{0.02\text{ M}})$  catalysts, respectively. In addition, unlike the  $\text{Cu}_5(\text{B}_{0.02\text{ M}})\text{Mg}_1$  catalyst which displays characteristic bands of  $^*\text{CO}$  and  $^*\text{CO}_2^-$  at  $-0.37\text{ V}$ , neither  $\text{Cu}_5\text{Mg}_1$  nor the  $\text{Cu}(\text{B}_{0.02\text{ M}})$  catalyst shows these bands until  $-0.47\text{ V}$ . Hence, it is evident that compared to the  $\text{Cu}_5\text{Mg}_1$  and  $\text{Cu}(\text{B}_{0.02\text{ M}})$  catalysts, the collaborative effect of Mg and B, which induces the formation of crystalline  $\text{Mg}(\text{OH})_2$  species in the catalyst structure, facilitates the early formation of  $^*\text{CO}_2^-$  and  $^*\text{CO}$  intermediates during the  $\text{CO}_2\text{RR}$ .

A previous study by Yang *et al.* utilized cerium as a self-sacrificing agent to stabilize  $\text{Cu}^+$  in their catalyst, taking advantage of the easy redox properties of  $\text{Ce}^{3+}/\text{Ce}^{4+}$ . Their *in situ* Raman and Fourier transform infrared spectroscopy results demonstrated that the stabilized  $\text{Cu}^+$  components promoted C-C coupling under the  $\text{CO}_2\text{RR}$ . DFT calculations further revealed that strong  $^*\text{CO}$  adsorption and low C-C coupling energy were conducive to the formation of  $\text{C}_2\text{H}_5\text{OH}$ .<sup>61</sup> Wang *et al.* prepared an ultra-thin 2D  $\text{Cu}_2\text{O}$  nanosheet ( $\text{Cu}_2\text{O-NS}$ ) catalyst with abundant oxygen vacancies. *In situ* Raman spectroscopy and DFT calculations supported that  $\text{Cu}_2\text{O-NS}$  prevented the reduction of surface Cu oxides, thereby stabilizing  $\text{Cu}^+$  and enhancing the conversion of  $\text{CO}_2$  to  $\text{C}_{2+}$ .<sup>68</sup> Similarly, in our work,  $\text{Cu}^+$  stabilization is achieved through the introduction of appropriate Mg and B into Cu materials. We found that the addition of the  $\text{NaBH}_4$  reactant can tune the amorphous or crystalline phases of  $\text{Mg}(\text{OH})_2$ . Crystallized  $\text{Mg}(\text{OH})_2$  is crucial for prolonging the lifetime of  $\text{Cu}^+$  during the  $\text{CO}_2\text{RR}$  and facilitating the activation of  $\text{CO}_2$  on the Cu surface to

generate key  $^*\text{CO}$  intermediates for C-C coupling. Consequently, this enhances the selectivity towards  $\text{C}_{2+}$  products of our catalyst.

### 3 Conclusion

Overall, a simple two-step method involving calcination and subsequent wet chemical reduction is developed to construct a Cu-based electrocatalyst modified by crystalline  $\text{Mg}(\text{OH})_2$  and B. XRD, TEM, and XPS analyses indicate that the addition of the  $\text{NaBH}_4$  reactant can induce the formation of crystalline  $\text{Mg}(\text{OH})_2$ , which is proposed to enhance the conversion of  $\text{CO}_2$  to  $\text{C}_{2+}$  during the  $\text{CO}_2\text{RR}$  compared to amorphous  $\text{Mg}(\text{OH})_2$ . In support of this, *in situ* Raman spectroscopy reveals that the synergy of crystalline  $\text{Mg}(\text{OH})_2$  and B can stabilize  $\text{Cu}^+$  at rather cathodic potentials during the  $\text{CO}_2\text{RR}$  process, effectively producing and preserving the  $^*\text{CO}$  intermediates, therefore greatly enhancing the  $^*\text{CO}-\text{CO}$  coupling. As a result, the  $\text{FE}_{\text{C}_{2+}}$  surpasses 60% on the  $\text{Cu}_5(\text{B}_{0.02\text{ M}})\text{Mg}_1$  electrocatalyst over a wide potential window of 600 mV ( $-1.17$  to  $-1.77\text{ V}$ ). In particular, at  $-1.57\text{ V}$ , the catalyst exhibits a  $\text{FE}_{\text{C}_{2+}}$  as high as 79.59%, demonstrating enormous potential for its scalable applications. This work not only provides a low-cost, simple and effective synthesis method for efficient electrocatalysts but also offers an in-depth understanding of the active sites and reaction intermediates during  $\text{CO}_2$ -to- $\text{C}_{2+}$  conversion. We believe that this will help inspire the rational design of future  $\text{CO}_2\text{RR}$  electrocatalysts.

### Conflicts of interest

The authors declare that they have no known competing financial interests or personal relationships that could have appeared to influence the work reported in this paper.

## Acknowledgements

The authors gratefully acknowledge the financial support from the National Natural Science Foundation of China (21905118 and 12304020), the Natural Science Foundation of Jiangsu Province (BK20230909), and the Funding for Scientific Research Startup of Jiangsu University (18JDG033).

## References

- 1 H. H. Wang, N. Wen, Y. Q. Wang, X. L. Jiao, Y. G. Xia and D. R. Chen, Boosting Electrochemical Reduction of  $\text{CO}_2$  to Formate over Oxygen Vacancy Stabilized Copper–Tin Dual Single Atoms Catalysts, *Adv. Funct. Mater.*, 2023, **33**, 2303473.
- 2 J. Y. Liu, P. S. Li, J. H. Bi, S. Q. Jia, Y. Wang, X. C. Kang, X. F. Sun, Q. G. Zhu and B. X. Han, Switching between  $\text{C}_{2+}$  Products and  $\text{CH}_4$  in  $\text{CO}_2$  Electrolysis by Tuning the Composition and Structure of Rare-Earth/Copper Catalysts, *J. Am. Chem. Soc.*, 2023, **145**, 23037–23047.
- 3 J. Yin, J. Jin, Z. Y. Yin, L. Zhu, X. Du, Y. Peng, P. Xi, C. H. Yan and S. H. Sun, The built-in electric field across  $\text{FeN}/\text{Fe}_3\text{N}$  interface for efficient electrochemical reduction of  $\text{CO}_2$  to  $\text{CO}$ , *Nat. Commun.*, 2023, **14**, 1724.
- 4 P. S. Li, J. H. Bi, J. Y. Liu, Y. Wang, X. C. Kang, X. F. Sun, J. L. Zhang, Z. M. Liu, Q. G. Zhu and B. X. Han, p-d Orbital Hybridization Induced by p-Block Metal-Doped Cu Promotes the Formation of  $\text{C}_{2+}$  Products in Ampere-Level  $\text{CO}_2$  Electroreduction, *J. Am. Chem. Soc.*, 2023, **145**, 4675–4682.
- 5 Z. Y. Zhang, H. Tian, L. Bian, S. Z. Liu, Y. Liu and Z. L. Wang, Cu-Zn-based alloy/oxide interfaces for enhanced electroreduction of  $\text{CO}_2$  to  $\text{C}_{2+}$  products, *J. Energy Chem.*, 2023, **83**, 90–97.
- 6 R. Shi, J. Guo, X. Zhang, G. I. N. Waterhouse, Z. Han, Y. Zhao, L. Shang, C. Zhou, L. Jiang and T. Zhang, Efficient wettability-controlled electroreduction of  $\text{CO}_2$  to  $\text{CO}$  at Au/C interfaces, *Nat. Commun.*, 2020, **11**, 3028.
- 7 X. T. Wang, Z. Z. Wang, Y. Li, J. T. Wang and G. K. Zhang, Efficient photocatalytic  $\text{CO}_2$  conversion over 2D/2D Ni-doped  $\text{CsPbBr}_3/\text{Bi}_3\text{O}_4\text{Br}$  Z-scheme heterojunction: Critical role of Ni doping, boosted charge separation and mechanism study, *Appl. Catal., B*, 2022, **319**, 121895.
- 8 J. Wu, Y. Huang, W. Ye and Y. Li,  $\text{CO}_2$  Reduction: From the Electrochemical to Photochemical Approach, *Adv. Sci.*, 2017, **4**, 1700194.
- 9 Z. Li, R. Wu, L. Zhao, P. Li, X. Wei, J. Wang, J. S. Chen and T. Zhang, Metal-support interactions in designing noble metal-based catalysts for electrochemical  $\text{CO}_2$  reduction: Recent advances and future perspectives, *Nano Res.*, 2021, **14**, 3795–3809.
- 10 Y. Yang, S. Louisia, S. M. Yu, J. B. Jin, I. Roh, C. B. Chen, M. V. F. Guzman, J. Feijoo, P. C. Chen, H. S. Wang, C. J. Pollock, X. Huang, Y. T. Shao, C. Wang, D. A. Muller, H. D. Abruña and P. D. Yang, Operando studies reveal active Cu nanograins for  $\text{CO}_2$  electroreduction, *Nature*, 2023, **614**, 262–269.
- 11 S. Y. Lee, J. M. Kim, G. Bak, E. C. Lee, D. Kim, S. Yoo, J. Kim, H. Yun and Y. J. Hwang, Probing Cation Effects on \*CO Intermediates from Electroreduction of  $\text{CO}_2$  through Operando Raman Spectroscopy, *J. Am. Chem. Soc.*, 2023, **145**, 23068–23075.
- 12 T. Ahmad, S. Liu, M. Sajid, K. Li, M. Ali, L. Liu and W. Chen, Electrochemical  $\text{CO}_2$  reduction to  $\text{C}_{2+}$  products using Cu-based electrocatalysts: A review, *Nano Res. Energy*, 2022, **1**, e9120021.
- 13 C. Liu, M. M. Wang, J. Y. Ye, L. B. Liu, L. G. Li, Y. H. Li and X. Q. Huang, Highly Selective  $\text{CO}_2$  Electroreduction to  $\text{C}_{2+}$  Products over  $\text{Cu}_2\text{O}$ -Decorated 2D Metal–Organic Frameworks with Rich Heterogeneous Interfaces, *Nano Lett.*, 2023, **23**, 1474–1480.
- 14 P. De Luna, R. Quintero-Bermudez, C. T. Dinh, M. B. Ross, O. S. Bushuyev, P. Todorović, T. Regier, S. O. Kelley, P. D. Yang and E. H. Sargent, Catalyst electro-redistribution controls morphology and oxidation state for selective carbon dioxide reduction, *Nat. Catal.*, 2018, **1**, 103–110.
- 15 L. C. Ding, N. N. Zhu, Y. Hu, Z. Chen, P. Song, T. Sheng, Z. C. Wu and Y. J. Xiong, Over 70% Faradaic Efficiency for  $\text{CO}_2$  Electroreduction to Ethanol Enabled by Potassium Dopant-Tuned Interaction between Copper Sites and Intermediates, *Angew. Chem., Int. Ed.*, 2022, **61**, e202209268.
- 16 C. Peng, G. Luo, J. B. Zhang, M. H. Chen, Z. Q. Wang, T. K. Sham, L. J. Zhang, Y. F. Li and G. F. Zheng, Double sulfur vacancies by lithium tuning enhance  $\text{CO}_2$  electroreduction to n-propanol, *Nat. Catal.*, 2021, **12**, 1580.
- 17 Y. R. Lin, D. U. Lee, S. Q. Tan, D. M. Koshy, T. Y. Lin, L. Wang, D. Corral, J. E. Avilés Acosta, J. A. Z. Zeledon, V. A. Beck, S. E. Baker, E. B. Duoss, C. Hahn and T. F. Jaramillo, Vapor-Fed Electrolyzers for Carbon Dioxide Reduction Using Tandem Electrocatalysts: Cuprous Oxide Coupled with Nickel–Coordinated Nitrogen-Doped Carbon, *Adv. Funct. Mater.*, 2022, **32**, 2113252.
- 18 X. P. Qin, S. Q. Zhu, F. Xiao, L. L. Zhang and M. H. Shao, Active Sites on Heterogeneous Single-Iron-Atom Electrocatalysts in  $\text{CO}_2$  Reduction Reaction, *ACS Energy Lett.*, 2019, **4**, 1778–1783.
- 19 Y. J. Shi, Y. J. Wang, J. Y. Yu, Y. K. Chen, C. Q. Fang, D. Jiang, Q. H. Zhang, L. Gu, X. W. Yu, X. Li, H. Liu and W. J. Zhou, Superscalar Phase Boundaries Derived Multiple Active Sites in  $\text{SnO}_2/\text{Cu}_6\text{Sn}_5/\text{CuO}$  for Tandem Electroreduction of  $\text{CO}_2$  to Formic Acid, *Adv. Energy Mater.*, 2023, **13**, 2203506.
- 20 P. T. Wang, M. Qiao, Q. Shao, Y. C. Pi, X. Zhu, Y. F. Li and X. Q. Huang, Phase and structure engineering of copper tin heterostructures for efficient electrochemical carbon dioxide reduction, *Nat. Catal.*, 2018, **9**, 4933.
- 21 D. G. Park, J. W. Choi, H. J. Chun, H. S. Jang, H. B. Lee, W. H. Choi, B. C. Moon, K. H. Kim, M. G. Kim, K. M. Choi, B. C. Han and J. K. Kang, Increasing CO Binding Energy and Defects by Preserving Cu Oxidation State via  $\text{O}_2$ -Plasma-Assisted N Doping on CuO Enables High  $\text{C}_{2+}$

Selectivity and Long-Term Stability in Electrochemical  $\text{CO}_2$  Reduction, *ACS Catal.*, 2023, **13**, 9222–9233.

22 G. Park, H. Kim, G. H. Han, J. Ha, J. Y. Seo, M. J. Kang, M. G. Seo, Y. H. Choi, S. Y. Kim and S. H. Ahn, The effect of Cu oxidation states on  $\text{C}_2\text{H}_4$  production from electrochemical  $\text{CO}_2$  conversion, *J. CO<sub>2</sub> Util.*, 2023, **75**, 102569.

23 R. B. Sun, C. Wei, Z. X. Huang, S. W. Niu, X. Han, C. Chen, H. R. Wang, J. Song, J. D. Yi, G. Wu, D. W. Rao, X. S. Zheng, Y. Wu, G. M. Wang and X. Hong,  $\text{Cu}_{2+1}\text{O}/\text{CuO}_x$  heterostructures promote the electrosynthesis of  $\text{C}_{2+}$  products from  $\text{CO}_2$ , *Nano Res.*, 2022, **16**, 4698–4705.

24 H. H. Yang, S. Y. Li and Q. Xu, Efficient strategies for promoting the electrochemical reduction of  $\text{CO}_2$  to  $\text{C}_{2+}$  products over Cu-based catalysts, *Chin. J. Catal.*, 2023, **48**, 32–65.

25 J. Wang, J. J. Liu, Y. Q. Song, S. B. Geng, Z. H. Peng, J. L. Yu, F. Liu, Y. H. Wang, S. B. Xi, Z. J. Zhang and Z. X. Fan, Simultaneous Defect and Size Control of Metal–Organic Framework Nanostructures for Highly Efficient Carbon Dioxide Electroreduction to Multicarbon Products, *ACS Mater. Lett.*, 2023, **5**, 2121–2130.

26 J. W. Su, D. H. Pan, Y. Dong, Y. Y. Zhang, Y. L. Tang, J. Sun, L. J. Zhang, Z. Q. Tian and L. Chen, Ultrafine  $\text{Fe}_2\text{C}$  Iron Carbide Nanoclusters Trapped in Topological Carbon Defects for Efficient Electroreduction of Carbon Dioxide, *Adv. Energy Mater.*, 2023, **13**, 2204391.

27 R. G. Cai, M. Z. Sun, F. Yang, M. Ju, Y. P. Chen, M. D. Gu, B. L. Huang and S. H. Yang, Engineering Cu(i)/Cu(0) interfaces for efficient ethanol production from  $\text{CO}_2$  electroreduction, *Chem.*, 2023, **10**, 1–23.

28 Y. P. Zang, T. F. Liu, P. F. Wei, H. F. Li, Q. Wang, G. X. Wang and X. H. Bao, Selective  $\text{CO}_2$  Electroreduction to Ethanol over a Carbon-Coated  $\text{CuO}_x$  Catalyst, *Angew. Chem., Int. Ed.*, 2022, **61**, e202209629.

29 C. F. Wen, M. Zhou, P. F. Liu, Y. W. Liu, X. F. Wu, F. X. Mao, S. Dai, B. B. Xu, X. L. Wang, Z. Jiang, P. Hu, S. Yang, H. F. Wang and H. G. Yang, Highly Ethylene-Selective Electrocatalytic  $\text{CO}_2$  Reduction Enabled by Isolated Cu–S Motifs in Metal–Organic Framework Based Precatalysts, *Angew. Chem., Int. Ed.*, 2021, **61**, e202111700.

30 Y. Yao, Y. Zhou, X. Liu, Y. Li, D. Wang, X. Chi, X. Wang, R. Zhao, H. Zhang, Y. Sun, Z.-Y. Yang, Y. Wei and Y.-M. Yan, Restraining lattice oxygen of  $\text{Cu}_2\text{O}$  by enhanced Cu–O hybridization for selective and stable production of ethylene with  $\text{CO}_2$  electroreduction, *J. Mater. Chem. A*, 2022, **10**, 20914–20923.

31 S. Sinha and J. J. Jiang, Main group elements in electrochemical hydrogen evolution and carbon dioxide reduction, *Chem. Commun.*, 2023, **59**, 11767–11779.

32 C. Peng, J. Ma, G. Luo, S. Yan, J. Zhang, Y. Chen, N. Chen, Z. Wang, W. Wei, T. K. Sham, Y. Zheng, M. Kuang and G. Zheng, (111) Facet-oriented  $\text{Cu}_2\text{Mg}$  Intermetallic Compound with  $\text{Cu}_3\text{-Mg}$  Sites for  $\text{CO}_2$  Electroreduction to Ethanol with Industrial Current Density, *Angew. Chem., Int. Ed. Engl.*, 2024, e202316907.

33 M. C. Xie, Y. Shen, W. C. Ma, D. Y. Wei, B. Zhang, Z. H. Wang, Y. H. Wang, Q. H. Zhang, S. J. Xie, C. Wang and Y. Wang, Fast Screening for Copper-Based Bimetallic Electrocatalysts: Efficient Electrocatalytic Reduction of  $\text{CO}_2$  to  $\text{C}_{2+}$  Products on Magnesium-Modified Copper, *Angew. Chem., Int. Ed.*, 2022, **61**, e202213423.

34 J. Fan, X. Zhang, M. Han, X. Xiang, C. Guo, Y. Lin, N. Shi, D. Xu, Y. Lai and J. Bao, Amorphous Ni–Fe–Mo Oxides Coupled with Crystalline Metallic Domains for Enhanced Electrocatalytic Oxygen Evolution by Promoted Lattice–Oxygen Participation, *Small*, 2023, **20**, 2303927.

35 Y. Z. Li, Z. B. Wang, C. Li, F. Qi, P. W. Yan, Y. P. Wang, M. F. He, Z. L. Chen, Q. Wang, Y. Wang, H. Zheng, A. Ikhlaq, J. Kumirska, E. Maria Siedlecka and O. Ismailova, Reducing agents enhanced prometon degradation by  $\text{CuBi}_2\text{O}_4$ /peroxyomonosulfate: Development of interfacial electron transport and circulation of  $\text{Cu}^+/\text{Cu}^{2+}$ , *Chem. Eng. J.*, 2023, **470**, 144387.

36 Z. P. Ma, T. Wan, D. Zhang, J. A. Yuwono, C. Tsounis, J. Jiang, Y. H. Chou, X. Y. Lu, P. V. Kumar, Y. H. Ng, D. Chu, C. Y. Toe, Z. J. Han and R. Amal, Atomically Dispersed Cu Catalysts on Sulfide-Derived Defective Ag Nanowires for Electrochemical  $\text{CO}_2$  Reduction, *ACS Nano*, 2023, **17**, 2387–2398.

37 Z. Q. Zhang, J. L. Liang, W. Zhang, M. Zhou, X. L. Zhu, Z. Y. Liu, Y. Li, Z. Q. Guan, C. S. Lee, P. K. Wong, H. M. Li and Z. F. Jiang, Modified-pollen confined hybrid system: A promising union for visible-light-driven photocatalytic antibiotic degradation, *Appl. Catal., B*, 2023, **330**, 122621.

38 X. L. Zhou, J. Q. Shan, L. Chen, B. Y. Xia, T. Ling, J. J. Duan, Y. Jiao, Y. Zheng and S. Z. Qiao, Stabilizing  $\text{Cu}^{2+}$  Ions by Solid Solutions to Promote  $\text{CO}_2$  Electroreduction to Methane, *J. Am. Chem. Soc.*, 2022, **144**, 2079–2084.

39 D. X. Tan, J. L. Zhang, L. Yao, X. N. Tan, X. Y. Cheng, Q. Wan, B. X. Han, L. R. Zheng and J. Zhang, Multi-shelled  $\text{CuO}$  microboxes for carbon dioxide reduction to ethylene, *Nano Res.*, 2020, **13**, 768–774.

40 V. Okatenko, A. Loiudice, M. A. Newton, D. C. Stoian, A. Blokhina, A. N. Chen, K. Rossi and R. Buonsanti, Alloying as a Strategy to Boost the Stability of Copper Nanocatalysts during the Electrochemical  $\text{CO}_2$  Reduction Reaction, *J. Am. Chem. Soc.*, 2023, **145**, 5370–5383.

41 P. T. Wang, H. Yang, C. Tang, Y. Wu, Y. Zheng, T. Cheng, K. Davey, X. Q. Huang and S. Z. Qiao, Boosting electrocatalytic  $\text{CO}_2$ -to-ethanol production via asymmetric C–C coupling, *Nat. Catal.*, 2022, **13**, 3754.

42 W. Lai, L. H. Ge, H. Yang, Y. L. Deng, H. M. Li, B. Ouyang, L. Xu and J. Bao, Reprogramming the redox states of nickel via interface engineering and heteroatom doping to boost overall water splitting, *J. Mater. Chem. A*, 2022, **10**, 10525–10539.

43 J. H. Jang, S. Q. Zhu, E. P. Delmo, T. H. Li, Q. L. Zhao, Y. N. Wang, L. L. Zhang, H. W. Huang, J. J. Ge and M. H. Shao, Facile design of oxide-derived Cu nanosheet electrocatalyst for  $\text{CO}_2$  reduction reaction, *EcoMat*, 2023, **5**, e12334.

44 Y. Zhang, Z. B. Si, H. H. Du, Y. L. Deng, Q. K. Zhang, Z. L. Wang, Q. Yu and H. Xu, Selective  $\text{CO}_2$  Reduction to

Ethylene Over a Wide Potential Window by Copper Nanowires with High Density of Defects, *Inorg. Chem.*, 2022, **61**, 20666–20673.

45 X.-J. Cui, Y.-Q. Qiu, H.-Q. Wang and C.-G. Liu, Direct coupling of two inert  $\text{CO}_2$  molecules to form a C–C bond on the  $\text{Cu}^0$  atomic interfaces of the nitrogen-doped graphene-supported  $\text{Cu}_4$  cluster, *Inorg. Chem. Front.*, 2024, **11**, 85–97.

46 G. M. Tomboc, S. Choi, T. Kwon, Y. J. Hwang and K. Lee, Potential Link between Cu Surface and Selective  $\text{CO}_2$  Electrocatalysis: Perspective on Future Electrocatalyst Designs, *Adv. Mater.*, 2020, **32**, e1908398.

47 Z. Li, Z. Liu, S. Li, Y. Pei, D. Li, J. Mao, R. Zhou, C. Qiu, Y. Lu and B. Zhang, Modulating the localized electronic distribution of Cu species during reconstruction for enhanced electrochemical  $\text{CO}_2$  reduction to  $\text{C}_{2+}$  products, *J. Mater. Chem. A*, 2024, DOI: [10.1039/d4ta01184h](https://doi.org/10.1039/d4ta01184h).

48 S. J. Han, L. L. Mao, T. Wu and H. Z. Wang, Homogeneous polyethersulfone hybrid membranes prepared with in-situ synthesized magnesium hydroxide nanoparticles by phase inversion method, *J. Membr. Sci.*, 2016, **516**, 47–55.

49 H. Zhang, D. Y. Zhang, M. Y. Guo, Z. Huang, X. Wang, C. Q. Gao, F. Gao, M. Terrones and Y. Q. Wang, Combustion Activation Induced Solid-State Synthesis for N, B Co-Doped Carbon/Zinc Borate Anode with a Boosting of Sodium Storage Performance, *Adv. Sci.*, 2023, **10**, 2207751.

50 H. Q. Peng, X. Ming, K. Pang, Y. R. Chen, J. Zhou, Z. Xu, Y. J. Liu and C. Gao, Highly electrically conductive graphene papers via catalytic graphitization, *Nano Res.*, 2022, **15**, 4902–4908.

51 J. Leverett, J. A. Yuwono, P. Kumar, T. Tran-Phu, J. Qu, J. Cairney, X. Wang, A. N. Simonov, R. K. Hocking, B. Johannessen, L. Dai, R. Daiyan and R. Amal, Impurity Tolerance of Unsaturated Ni-N-C Active Sites for Practical Electrochemical  $\text{CO}_2$  Reduction, *ACS Energy Lett.*, 2022, **7**, 920–928.

52 S. Van Daele, L. Hintjens, S. Hoekx, B. Bohlen, S. Neukermans, N. Daems, J. Hereijgers and T. Breugelmans, How flue gas impurities affect the electrochemical reduction of  $\text{CO}_2$  to CO and formate, *Appl. Catal., B*, 2024, **341**, 123345.

53 W. Lai, Y. Qiao, Y. Wang and H. Huang, Stability Issues in Electrochemical  $\text{CO}_2$  Reduction: Recent Advances in Fundamental Understanding and Design Strategies, *Adv. Mater.*, 2023, **35**, e2306288.

54 G. X. Zhang, X. L. Zheng, X. M. Cui, J. Wang, J. H. Liu, J. F. Chen and Q. Xu, Doping of Vanadium into Bismuth Oxide Nanoparticles for Electrocatalytic  $\text{CO}_2$  Reduction, *ACS Appl. Nano Mater.*, 2022, **5**, 15465–15472.

55 D. Ren, Y. L. Deng, A. D. Handoko, C. S. Chen, S. Malkhandi and B. S. Yeo, Selective Electrochemical Reduction of Carbon Dioxide to Ethylene and Ethanol on Copper(I) Oxide Catalysts, *ACS Catal.*, 2015, **5**, 2814–2821.

56 S. J. Mu, H. L. Lu, Q. B. Wu, L. Li, R. I. Zhao, C. Long and C. H. Cui, Hydroxyl radicals dominate reoxidation of oxide-derived Cu in electrochemical  $\text{CO}_2$  reduction, *Nat. Commun.*, 2022, **13**, 3694.

57 H. T. Du, L. X. Liu, P. Li, Q. H. Min, S. J. Guo and W. L. Zhu, Enriching Reaction Intermediates in Multishell Structured Copper Catalysts for Boosted Propanol Electrosynthesis from Carbon Monoxide, *ACS Nano*, 2023, **17**, 8663–8670.

58 Y. Zhao, X. G. Zhang, N. Bodappa, W. M. Yang, Q. Liang, P. M. Radjenovic, Y. H. Wang, Y. J. Zhang, J. C. Dong, Z. Q. Tian and J. F. Li, Elucidating electrochemical  $\text{CO}_2$  reduction reaction processes on  $\text{Cu}(hkl)$  single-crystal surfaces by in situ Raman spectroscopy, *Energy Environ. Sci.*, 2022, **15**, 3968–3977.

59 Y. L. Deng, Y. Huang, D. Ren, A. D. Handoko, Z. W. Seh, P. Hirunsit and B. S. Yeo, On the Role of Sulfur for the Selective Electrochemical Reduction of  $\text{CO}_2$  to Formate on  $\text{CuS}_x$  Catalysts, *ACS Appl. Mater. Interfaces*, 2018, **10**, 28572–28581.

60 D. Ren, J. H. Fong and B. S. Yeo, The effects of currents and potentials on the selectivities of copper toward carbon dioxide electroreduction, *Nat. Commun.*, 2018, **9**, 925.

61 Z. Yang, D. G. Ji, Z. Li, Z. D. He, Y. Hu, J. Yin, Y. H. Hou, P. X. Xi and C. H. Yan,  $\text{CeO}_2/\text{CuS}$  Nanoplates Electroreduce  $\text{CO}_2$  to Ethanol with Stabilized  $\text{Cu}^+$  Species, *Small*, 2023, **19**, 2303099.

62 X. P. Yan, M. L. Zhang, Y. Z. Chen, Y. H. Wu, R. Z. Wu, Q. Wan, C. X. Liu, T. T. Zheng, R. J. Feng, J. Zhang, C. J. Chen, C. Xia, Q. G. Zhu, X. F. Sun, Q. L. Qian and B. X. Han, Synergy of  $\text{Cu}/\text{C}_3\text{N}_4$  Interface and Cu Nanoparticles Dual Catalytic Regions in Electrolysis of CO to Acetic Acid, *Angew. Chem., Int. Ed.*, 2023, **62**, e202301507.

63 R. Amirbeigiarab, J. Tian, A. Herzog, C. R. Qiu, A. Bergmann, B. R. Cuenya and O. M. Magnussen, Atomic-scale surface restructuring of copper electrodes under  $\text{CO}_2$  electroreduction conditions, *Nat. Catal.*, 2023, **6**, 837–846.

64 H. Zhang, Y. Qiao, Y. Wang, Y. Zheng and H. Huang, In situ oxidative etching-enabled synthesis of hollow  $\text{Cu}_2\text{O}$  nanocrystals for efficient  $\text{CO}_2\text{RR}$  into  $\text{C}_{2+}$  products, *Sustainable Energy Fuels*, 2022, **6**, 4860–4865.

65 M. Fang, M. Wang, Z. Wang, Z. Zhang, H. Zhou, L. Dai, Y. Zhu and L. Jiang, Hydrophobic, Ultrastable  $\text{Cu}^{\delta+}$  for Robust  $\text{CO}_2$  Electroreduction to  $\text{C}_2$  Products at Ampere-Current Levels, *J. Am. Chem. Soc.*, 2023, **145**, 11323–11332.

66 Y. Zhou, Y. Yao, R. Zhao, X. Wang, Z. Fu, D. Wang, H. Wang, L. Zhao, W. Ni, Z. Yang and Y. M. Yan, Stabilization of  $\text{Cu}^+$  via Strong Electronic Interaction for Selective and Stable  $\text{CO}_2$  Electroreduction, *Angew. Chem., Int. Ed.*, 2022, **61**, e202205832.

67 H. Cheng, S. Jia, J. Jiao, X. Chen, T. Deng, C. Xue, M. Dong, J. Zeng, C. Chen, H. Wu, M. He and B. Han, Stabilization of  $\text{Cu}^+$  sites by amorphous  $\text{Al}_2\text{O}_3$  to enhance electrochemical  $\text{CO}_2$  reduction to  $\text{C}_{2+}$  products, *Green Chem.*, 2024, **26**, 2599–2604.

68 P. Wang, S. Meng, B. Zhang, M. He, P. Li, C. Yang, G. Li and Z. Li, Sub-1 nm  $\text{Cu}_2\text{O}$  Nanosheets for the Electrochemical  $\text{CO}_2$  Reduction and Valence State-Activity Relationship, *J. Am. Chem. Soc.*, 2023, **145**, 26133–26143.